The Astrophysical Journal, 814:60 (14pp), 2015 November 20 doi:10.1088/0004-637X/814/1/60

KINK AND SAUSAGE MODES IN NONUNIFORM MAGNETIC SLABS WITH CONTINUOUS TRANSVERSE DENSITY DISTRIBUTIONS

Hui Yu, Bo Li, Shao-Xia Chen, and Ming-Zhe Guo
Shandong Provincial Key Laboratory of Optical Astronomy and Solar-Terrestrial Environment,
Institute of Space Sciences, Shandong University, Weihai, 264209, China; bbl@sdu.edu.cn
Received 2015 September 22; accepted 2015 October 19; published 2015 November 17

ABSTRACT

We examine the influence of a continuous density structuring transverse to coronal slabs on the dispersive properties of fundamental standing kink and sausage modes supported therein. We derive generic dispersion relations (DRs) governing linear fast waves in pressureless straight slabs with general transverse density distributions, and focus on cases where the density inhomogeneity takes place in a layer of arbitrary width and in arbitrary form. The physical relevance of the solutions to the DRs is demonstrated by the corresponding time-dependent computations. For all profiles examined, the lowest order kink modes are trapped regardless of longitudinal wavenumber k. A continuous density distribution introduces a difference to their periods of $\lesssim 13\%$ when k is the observed range relative to the case where the density profile takes a step function form. Sausage modes and other branches of kink modes are leaky at small k, and their periods and damping times are heavily influenced by how the transverse density profile is prescribed, in particular the length scale. These modes have sufficiently high quality to be observable only for physical parameters representative of flare loops. We conclude that while the simpler DR pertinent to a step function profile can be used for the lowest order kink modes, the detailed information on the transverse density structuring needs to be incorporated into studies of sausage modes and higher order kink modes.

Key words: magnetohydrodynamics (MHD) – Sun: corona – Sun: flares – Sun: magnetic fields – waves

1. INTRODUCTION

Considerable progress has been made in recent years in the field of solar magneto-seismology (see Ballester et al. 2007; Nakariakov & Erdélyi 2009; Erdélyi & Goossens 2011 for three recent topical issues). This is made possible due to the abundant measurements of low-frequency waves and oscillations in a rich variety of atmospheric structures on the Sun (for recent reviews, see, e.g., Nakariakov & Verwichte 2005; Banerjee et al. 2007; De Moortel & Nakariakov 2012). Equally important is a refined theoretical understanding of the collective waves in a structured magnetic environment, which was built on the original ideas put forward in the 1970s and 1980s (notably Rosenberg 1970; Uchida 1970; Zajtsev & Stepanov 1975; Roberts et al. 1984). A combination of theories and observations then enables the inference of solar atmospheric parameters that prove difficult to measure directly. Take the two most studied transverse waves in the corona, the fast kink and sausage waves, for instance. The periods of standing kink modes can offer key information on the magnetic field strength in coronal loops (e.g., Roberts et al. 1984; Nakariakov & Ofman 2001; Erdélyi & Taroyan 2008; Ofman & Wang 2008; White & Verwichte 2012). Their damping times can help infer the transverse density structuring (e.g., Ruderman & Roberts 2002; Arregui et al. 2007; Goossens et al. 2008), given that this damping is mostly attributable to resonant absorption (see Goossens et al. 2011 for a review). On the other hand, sausage modes were suggested to be responsible for causing a substantial fraction of quasi-periodic pulsations (QPPs) in the light curves of solar flares (e.g., Nakariakov & Melnikov 2009). Their periods and damping times can be employed to yield the magnetic field strength in the key region where flare energy is released, as well as the transverse density inhomogeneity of flare loops (e.g., Nakariakov et al. 2003, 2012; Chen et al. 2015b).

Fast kink and sausage modes supported by coronal cylinders are rather well understood. If the physical parameters are transversally structured in a piecewise constant (step function) fashion, the lowest order kink modes are trapped regardless of longitudinal wavenumber k, whereas sausage modes, as well as other branches of kink modes, are trapped only when k exceeds some cutoff value (e.g., Edwin & Roberts 1983). In the leaky regime, the wave energy is not well confined to coronal cylinders but is transmitted into their surroundings (e.g., Spruit 1982; Cally 1986). In addition, the sausage mode period (damping time) is known to increase (decrease) with decreasing k, and becomes k-independent when k is sufficiently small (Kopylova et al. 2007; Vasheghani Farahani et al. 2014). If the cylinders are continuously structured in the transverse direction, the first branch of kink modes becomes resonantly coupled to torsional Alfvén waves and experiences temporal damping as well (Goossens et al. 2002; Ruderman & Roberts 2002, and also Hollweg & Yang 1988). Their damping times show some considerable dependence on the length scale, or equivalently the steepness, of the transverse density distribution (e.g., Soler et al. 2014). On the other hand, while the k dependence of the sausage mode periods P and damping times τ is reminiscent of the step function case, the values of P (Nakariakov et al. 2012; Li et al. 2014; Chen et al. 2015a) and τ (Chen et al. 2015b) may be sensitive to the transverse density structuring. Indeed, this profile dependence has inspired us (Chen et al. 2015b, hereafter Paper I) to construct a scheme for inferring flare loop parameters, in particular the transverse density length scale, with QPP measurements.

Initiated in the comprehensive studies by Roberts (1981a) and Edwin & Roberts (1982), a considerable number of investigations into collective waves in coronal slabs are also available. On the one hand, waves in slabs are easier to handle mathematically, and their examination can provide a useful guide to what one may encounter in examining waves in cylinders. On the other hand, while waves in slabs are usually expected to be less applicable to observations in the solar atmosphere, in some situations a slab geometry was considered to be more relevant. For instance, fast sausage waves in slabs were employed to account for the sunward moving tadpoles in post-flare super arcades measured with the Transition Region and Coronal Explorer (TRACE; Verwichte et al. 2005). Likewise, the large-scale propagating disturbances in streamer stalks, as seen in images obtained with the Large Angle and Spectrometric Coronagraph on board the *Solar and Heliospheric Observatory* satellite, were interpreted in terms of fast kink waves supported by magnetic slabs (Chen et al. 2010, 2011). Interestingly, the theoretical results of fast collective waves supported by slabs are also applicable even in the presence of current sheets (Edwin et al. 1986; Smith et al. 1997; Feng et al. 2011; Hornsey et al. 2014). As a matter of fact, fast sausage waves supported by current sheets were suggested to be responsible for some fine structures in broadband type IV radio bursts (e.g., Karlický et al. 2013).

There seems to be an apparent lack of a systematic study on how continuous transverse structuring influences the dispersive properties of fast waves in coronal slabs. Besides the step function case, only a limited number of analytical dispersion relations (DRs) are available for the continuous density profiles of some specific form (Edwin & Roberts 1988; Nakariakov & Roberts 1995; Lopin & Nagorny 2015). On the other hand, numerical studies from an initial value problem perspective are primarily interested in the time signatures of fast waves in slabs with some prescribed continuous density profiles (Murawski & Roberts 1993; Nakariakov et al. 2004; Hornsey et al. 2014). In the cylindrical case, however, analytical DRs are now available for transverse density distributions that are essentially arbitrary, and systematic investigations into the associated effects are available for both kink (Soler et al. 2013, 2014) and sausage modes (Paper I). One naturally asks: is a similar practice possible in the slab geometry? The present study aims to present such a practice. To this end, we will derive an analytical DR governing linear fast waves hosted by magnetized slabs with a rather general transverse density distribution. The only requirement here is that the density is uniform beyond some distance from a slab. However, the density profile within this distance is allowed to be in arbitrary form and of arbitrary steepness. Mathematically, this derivation largely follows Paper I and capitalizes on the fact that when fast waves are restricted to be in the plane containing the slab axis and the direction of density inhomogeneity, neither kink nor sausage waves resonantly couple to shear Alfvén waves. Regular series expansions about some point located in the inhomogeneous part of the density distribution can then be used to describe fast wave perturbations.

This manuscript is organized as follows. Section 2 presents the derivation of the DR together with our solution method. A parameter study is then presented in Section 3 to examine how the periods and damping times of fast waves depend on the slab parameters, in particular the steepness of the transverse density profile, for a number of different profile prescriptions. Finally, Section 4 gives our summary and some concluding remarks.

2. MATHEMATICAL FORMULATION

2.1. *Description for Equilibrium Slabs*

We model coronal structures as straight, density-enhanced slabs of half-width R and aligned with a uniform magnetic field $\boldsymbol{B} = B\hat{z}$. The equilibrium density ρ is assumed to be inhomogeneous only in the x-direction, and $\rho(x)$ is an even function. Apart from this, the only requirement is that ρ is uniform beyond some distance from the slab, making our analysis applicable to a wide variety of density profiles. In the majority of our study, we examine the profiles that can be decomposed into a uniform core with density $\rho_{\rm i}$, a uniform external medium with density $\rho_{\rm e}$, and a transition layer connecting the two ($\rho_{\rm i} > \rho_{\rm e}$). In other words,

$$\rho(x) = \begin{cases} \rho_{\rm i}, & 0 \leqslant x \leqslant x_{\rm i} = R - l/2, \\ \rho_{\rm tr}(x), & x_{\rm i} \leqslant x \leqslant x_{\rm e} = R + l/2, \\ \rho_{\rm e}, & x \geqslant x_{\rm e}, \end{cases} \tag{1}$$

where the thickness (l) of this transition layer is bounded by 0 and $2R$, corresponding to the steepest and least steep cases, respectively. In Appendix B, we will show that our analysis can be readily extended to profiles without a uniform core.

Similar to Paper I, we examine the following profiles

$$\rho_{\rm tr}(x) = \begin{cases} \rho_{\rm i} - \dfrac{\rho_{\rm i} - \rho_{\rm e}}{l}(x - x_{\rm i}), & \text{linear}, \\ \rho_{\rm i} - \dfrac{\rho_{\rm i} - \rho_{\rm e}}{l^2}(x - x_{\rm i})^2, & \text{parabolic}, \\ \rho_{\rm e} - \dfrac{\rho_{\rm e} - \rho_{\rm i}}{l^2}(x - x_{\rm e})^2, & \text{inverse-parabolic}, \\ \dfrac{\rho_{\rm i}}{2}\left[(1 + \dfrac{\rho_{\rm e}}{\rho_{\rm i}}) \right. \\ \left. -(1 - \dfrac{\rho_{\rm e}}{\rho_{\rm i}})\sin\dfrac{\pi(x - R)}{l}\right], & \text{sine} \end{cases} \tag{2}$$

We note that the sine profile was first introduced by Ruderman & Roberts (2002) when examining the effect of resonant absorption in damping standing kink modes in transversally nonuniform coronal cylinders. Our analysis of fast waves is valid for arbitrary prescriptions of $\rho_{\rm tr}(x)$, and the specific profiles are chosen here only to allow for a quantitative analysis. Figure 1 shows the x-dependence of the chosen ρ profiles, where $\rho_{\rm i}/\rho_{\rm e}$ and l/R are chosen to be 10 and 1, respectively, for illustration purposes.

2.2. *Solutions for Transverse Lagrangian Displacement and Total Pressure Perturbation*

Appropriate for the solar corona, we adopt the framework of cold (zero-β) MHD. In addition, we consider only fast waves in the x–z plane by letting $\partial/\partial y \equiv 0$. Let $\delta\boldsymbol{v}$ and $\delta\boldsymbol{b}$ denote the velocity and magnetic field perturbations, respectively. One finds that δv_y, δv_z, and δb_y vanish. The perturbed magnetic pressure, or equivalently total pressure in this zero-β case, is $\delta p_{\rm tot} = B\delta b_z/4\pi$. Fourier decomposing any perturbed value

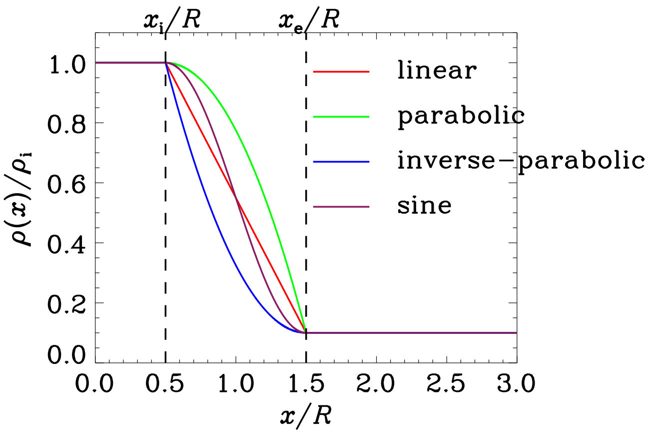

Figure 1. Transverse equilibrium density profiles as a function of x. The profiles differ only in how they are described in a transition layer connecting the internal (ρ_i) and external (ρ_e) values. For illustration purposes, ρ_i/ρ_e is chosen to be 10, and the width of this transition layer (l) is chosen to equal the slab half-width (R).

$\delta f(x, z, t)$ as

$$\delta f(x, z, t) = \mathrm{Re}\left\{\tilde{f}(x)\exp[-i(\omega t - kz)]\right\}, \tag{3}$$

one finds from linearized, ideal, cold MHD equations that

$$\frac{d^2\tilde{\xi}_x}{dx^2} + \left(\frac{\omega^2}{v_A^2} - k^2\right)\tilde{\xi}_x = 0. \tag{4}$$

Here $\tilde{\xi}_x = i\tilde{v}_x/\omega$ is the Fourier amplitude of the transverse Lagrangian displacement, and $v_A(x) = B/\sqrt{4\pi\rho(x)}$ is the Alfvén speed. The Fourier amplitude of the perturbed total pressure is

$$\tilde{p}_{\mathrm{tot}} = -\frac{B^2}{4\pi}\frac{d\tilde{\xi}_x}{dx}. \tag{5}$$

We note that Equations (4) and (5) can be derived by letting the sound speeds vanish in the finite β expressions given by Roberts (1981b, Equations (16) and (18) therein).

Evidently, the equations governing fast waves (see Equation (4)) do not contain any singularity. This is different from the cylindrical case where a treatment of singularity is necessary to address the resonant coupling of kink waves to torsional Alfvén waves (e.g., Soler et al. 2013, and references therein). Mathematically, the solutions to Equation (4) in the transition layer can be expressed as linear combinations of two linearly independent solutions, $\xi_{\mathrm{tr},1}$ and $\xi_{\mathrm{tr},2}$, which are regular series expansions about $\zeta \equiv x - R = 0$. In other words,

$$\tilde{\xi}_{\mathrm{tr},1}(\zeta) = \sum_{n=0}^{\infty} a_n\zeta^n,\ \tilde{\xi}_{\mathrm{tr},2}(\zeta) = \sum_{n=0}^{\infty} b_n\zeta^n. \tag{6}$$

Without loss of generality, one may choose

$$a_0 = R,\ a_1 = 0,\ b_0 = 0,\ b_1 = 1. \tag{7}$$

To determine the coefficients $[a_n, b_n]$ for $n \geqslant 2$, we expand $\rho_{\mathrm{tr}}(x)$ about $\zeta = 0$ as well, resulting in

$$\rho_{\mathrm{tr}}(\zeta) = \rho_0 + \sum_{n=1}^{\infty}\rho_n\zeta^n, \tag{8}$$

where

$$\rho_0 = \rho\ |_{\zeta=0},\ \text{and}\ \rho_n = \frac{1}{n!}\frac{d^n\rho(\zeta)}{d\zeta^n}\bigg|_{\zeta=0}\ (n \geqslant 1). \tag{9}$$

Now substituting Equation (6) into Equation (4) with the change of independent variable from x to ζ, one arrives at

$$\chi_n = -\frac{1}{n(n-1)}\left[\frac{4\pi\omega^2}{B^2}\sum_{l=0}^{n-2}\rho_{n-2-l}\chi_l - k^2\chi_{n-2}\right]\ (n \geqslant 2), \tag{10}$$

where χ represents either a or b.

The Fourier amplitude of the transverse Lagrangian displacement reads

$$\tilde{\xi}_x(x) = \begin{cases} \begin{cases} A_i \sin(\mu_i x), & \text{sausage} \\ A_i \cos(\mu_i x), & \text{kink} \end{cases}, & 0 \leqslant x \leqslant x_i, \\ A_1\tilde{\xi}_{\mathrm{tr},1}(\zeta) + A_2\tilde{\xi}_{\mathrm{tr},2}(\zeta), & x_i < x < x_e, \\ A_e \exp(i\mu_e x), & x \geqslant x_e, \end{cases} \tag{11}$$

where A_i, A_e, A_1, and A_2 are arbitrary constants. In addition,

$$\mu_{i,e} = \sqrt{\frac{\omega^2}{v_{Ai,e}^2} - k^2}\left(-\frac{\pi}{2} < \arg\mu_{i,e} \leqslant \frac{\pi}{2}\right), \tag{12}$$

with $v_{Ai,e}^2 = B^2/(4\pi\rho_{i,e})$. With the aid of Equation (5), the Fourier amplitude of the total pressure perturbation evaluates to

$$\tilde{p}_{\mathrm{tot}}(x) = -\frac{B^2}{4\pi} \times \begin{cases} \begin{cases} A_i\mu_i \cos(\mu_i x), & \text{sausage} \\ -A_i\mu_i \sin(\mu_i x), & \text{kink} \end{cases}, & 0 \leqslant x \leqslant x_i, \\ A_1\tilde{\xi}_{\mathrm{tr},1}'(\zeta) + A_2\tilde{\xi}_{\mathrm{tr},2}'(\zeta), & x_i < x < x_e, \\ iA_e\mu_e \exp(i\mu_e x), & x \geqslant x_e, \end{cases} \tag{13}$$

where the prime $' = d/d\zeta$.

A few words are necessary to address the restriction on arg $\mu_{i,e}$. As will be obvious in the derived DR, allowing μ_i to take the negative square root in Equation (12) will not introduce additional independent solutions. On the other hand, the restriction on arg μ_e excludes the unphysical solutions that correspond to purely growing perturbations (with μ_e lying on the negative imaginary axis) in the external medium (see Terradas et al. 2005 for a discussion on these unphysical solutions). This restriction also allows a unified examination of both trapped and leaky waves. Indeed, the trapped regime arises when $\arg\mu_e = \pi/2$, in which case one finds that $\exp(i\mu_e x) = \exp(-|\mu_e|x)$. For a similar discussion in the cylindrical case, see Cally (1986).

2.3. DRs of Fast Waves

The DRs governing linear fast waves follow from the requirement that both $\tilde{\xi}_x$ and $\tilde{p}_{\mathrm{tot}}$ must be continuous at the interfaces $x = x_\mathrm{i}$ and $x = x_\mathrm{e}$. This leads to

$$A_1\tilde{\xi}_{\mathrm{tr},1}(\zeta_\mathrm{i}) + A_2\tilde{\xi}_{\mathrm{tr},2}(\zeta_\mathrm{i}) = \begin{cases} A_\mathrm{i}\sin(\mu_\mathrm{i} x_\mathrm{i}), & \text{sausage} \\ A_\mathrm{i}\cos(\mu_\mathrm{i} x_\mathrm{i}), & \text{kink} \end{cases},$$

$$A_1\tilde{\xi}_{\mathrm{tr},1}(\zeta_\mathrm{e}) + A_2\tilde{\xi}_{\mathrm{tr},2}(\zeta_\mathrm{e}) = A_\mathrm{e}\exp(i\mu_\mathrm{e} x_\mathrm{e})$$

$$A_1\tilde{\xi}'_{\mathrm{tr},1}(\zeta_\mathrm{i}) + A_2\tilde{\xi}'_{\mathrm{tr},2}(\zeta_\mathrm{i}) = \begin{cases} A_\mathrm{i}\mu_\mathrm{i}\cos(\mu_\mathrm{i} x_\mathrm{i}), & \text{sausage} \\ -A_\mathrm{i}\mu_\mathrm{i}\sin(\mu_\mathrm{i} x_\mathrm{i}), & \text{kink} \end{cases},$$

$$A_1\tilde{\xi}'_{\mathrm{tr},1}(\zeta_\mathrm{e}) + A_2\tilde{\xi}'_{\mathrm{tr},2}(\zeta_\mathrm{e}) = iA_\mathrm{e}\mu_\mathrm{e}\exp(i\mu_\mathrm{e} x_\mathrm{e})$$

where $\zeta_\mathrm{i} = -l/2$ and $\zeta_\mathrm{e} = l/2$. Eliminating A_i (A_e), one finds that

$$\begin{aligned} \Lambda_1 A_1 + \Lambda_2 A_2 &= 0, \\ \Lambda_3 A_1 + \Lambda_4 A_2 &= 0, \end{aligned} \tag{14}$$

where the coefficients read

$$\begin{aligned} \Lambda_1 &= X_\mathrm{i}\tilde{\xi}_{\mathrm{tr},1}(\zeta_\mathrm{i}) - \tilde{\xi}'_{\mathrm{tr},1}(\zeta_\mathrm{i}),\ \Lambda_2 = X_\mathrm{i}\tilde{\xi}_{\mathrm{tr},2}(\zeta_\mathrm{i}) - \tilde{\xi}'_{\mathrm{tr},2}(\zeta_\mathrm{i}), \\ \Lambda_3 &= X_\mathrm{e}\tilde{\xi}_{\mathrm{tr},1}(\zeta_\mathrm{e}) - \tilde{\xi}'_{\mathrm{tr},1}(\zeta_\mathrm{e}),\ \Lambda_4 = X_\mathrm{e}\tilde{\xi}_{\mathrm{tr},2}(\zeta_\mathrm{e}) - \tilde{\xi}'_{\mathrm{tr},2}(\zeta_\mathrm{e}), \end{aligned} \tag{15}$$

with

$$X_\mathrm{e} = i\mu_\mathrm{e},\ X_\mathrm{i} = \begin{cases} \mu_\mathrm{i}\cot(\mu_\mathrm{i} x_\mathrm{i}), & \text{sausage} \\ -\mu_\mathrm{i}\tan(\mu_\mathrm{i} x_\mathrm{i}), & \text{kink} \end{cases} \tag{16}$$

Evidently, for Equation (14) to allow non-trivial solutions of $[A_1, A_2]$, one needs to require that

$$\Lambda_1\Lambda_4 - \Lambda_2\Lambda_3 = 0, \tag{17}$$

which is the DR we are looking for.

In the limit $l/R \to 0$, Equation (17) should recover the well-known results for the step function profile. This can be readily shown by retaining only terms to the 0th order in l/R and by noting that $x_\mathrm{i} \approx x_\mathrm{e} \approx R$. The coefficients Λ_n ($n = 1, \ldots, 4$) simplify to

$$\begin{aligned} \Lambda_1 &= X_\mathrm{i} a_0 - a_1, \\ \Lambda_2 &= X_\mathrm{i} b_0 - b_1, \\ \Lambda_3 &= X_\mathrm{e} a_0 - a_1, \\ \Lambda_4 &= X_\mathrm{e} b_0 - b_1. \end{aligned}$$

Substituting these expressions into Equation (17), one finds that

$$(X_\mathrm{i} - X_\mathrm{e})(a_1 b_0 - a_0 b_1) = 0.$$

Now that $a_1 b_0 - a_0 b_1$ cannot be zero since $\tilde{\xi}_{\mathrm{tr},1}$ and $\tilde{\xi}_{\mathrm{tr},2}$ are linearly independent, one finds that $X_\mathrm{i} = X_\mathrm{e}$. To be specific (see Equation (16)),

$$\begin{cases} i\mu_\mathrm{e} = \mu_\mathrm{i}\cot(\mu_\mathrm{i} R), & \text{sausage} \\ i\mu_\mathrm{e} = -\mu_\mathrm{i}\tan(\mu_\mathrm{i} R), & \text{kink} \end{cases} \tag{18}$$

which is the DR for step function density profiles (e.g., Terradas et al. 2005; Li et al. 2013).

Before proceeding, we note that the DR is valid for both propagating and standing waves. Throughout this study, however, we focus on standing modes by assuming that the longitudinal wavenumber k is real, whereas the angular frequency ω can be complex-valued. In addition, wherever applicable, we examine only fundamental modes, namely, the modes with $k = \pi/L$ where L is the slab length. Once a choice for ρ_tr is made, ω in units of v_Ai/R depends only on the dimensionless parameters $[\rho_\mathrm{i}/\rho_\mathrm{e}, l/R, kR]$. A numerical approach is then necessary to solve the DR (Equation (17)). For this purpose, we start with evaluating the coefficients ρ_n with Equation (9), and then evaluate a_n and b_n with Equation (10). The coefficients Λ_n can be readily obtained with Equations (15) and (16), thereby allowing us to solve Equation (17). When evaluating Λ_n, we truncate the infinite series expansion in Equation (6) by retaining only the terms with n up to $N = 101$. A convergence test has been made for a substantial fraction of the numerical results to make sure that using an even larger N does not introduce any appreciable difference.

Given that a numerical approach is needed after all, one may ask why we do not treat the problem numerically from the outset. Let us address this issue by comparing our approach with two representative fully numerical methods for examining the dispersive properties of fast modes. First, one may solve Equation (4) as an eigenvalue problem with a chosen $v_\mathrm{A}(x)$ profile (e.g., Pascoe et al. 2007; Jelínek & Karlický 2012; Li et al. 2014). However, this approach usually needs to specify the outer boundary condition that the Lagrangian displacement $\tilde{\xi}$ vanishes, and therefore can be used only to examine trapped modes since $\tilde{\xi}$ diverges rather than vanishing for leaky modes at large distances. Second, one may obtain a time-dependent equation governing, say, the transverse velocity perturbation and find the periods and damping times of fast modes by analyzing the temporal evolution of the perturbation signals (see Appendix A for details). Compared with this approach, solving the analytical DR is substantially less computationally expensive, thereby allowing an exhaustive parameter study to be readily conducted. On top of that, the periods and damping times for heavily damped modes can be easily evaluated, whereas the perturbation signals may decay too rapidly to permit their proper determination.

For future reference, we note that Equation (18) allows one to derive explicit expressions for ω at $k = 0$ and for the critical wavenumber k_c that separates the leaky from trapped regimes (Terradas et al. 2005, Equations (8) to (13)). With our notations, the results for sausage modes can be expressed as

$$\begin{aligned} k_\mathrm{c} &= \frac{1}{R}\frac{(n + 1/2)\pi}{\sqrt{v_\mathrm{Ae}^2/v_\mathrm{Ai}^2 - 1}}, \\ \omega_\mathrm{R} &= \frac{v_\mathrm{Ai}}{R}\left(n + \frac{1}{2}\right)\pi, \\ \omega_\mathrm{I} &= -\frac{v_\mathrm{Ai}}{2R}\ln\frac{1 + v_\mathrm{Ai}/v_\mathrm{Ae}}{1 - v_\mathrm{Ai}/v_\mathrm{Ae}}, \end{aligned} \tag{19}$$

where $n = 0, 1, \ldots$. Similarly, the results for kink modes read

$$\begin{aligned} k_\mathrm{c} &= \frac{1}{R}\frac{n\pi}{\sqrt{v_\mathrm{Ae}^2/v_\mathrm{Ai}^2 - 1}}, \\ \omega_\mathrm{R} &= \frac{v_\mathrm{Ai}}{R}n\pi, \\ \omega_\mathrm{I} &= -\frac{v_\mathrm{Ai}}{2R}\ln\frac{1 + v_\mathrm{Ai}/v_\mathrm{Ae}}{1 - v_\mathrm{Ai}/v_\mathrm{Ae}}, \end{aligned} \tag{20}$$

where $n = 1, 2, \ldots$.

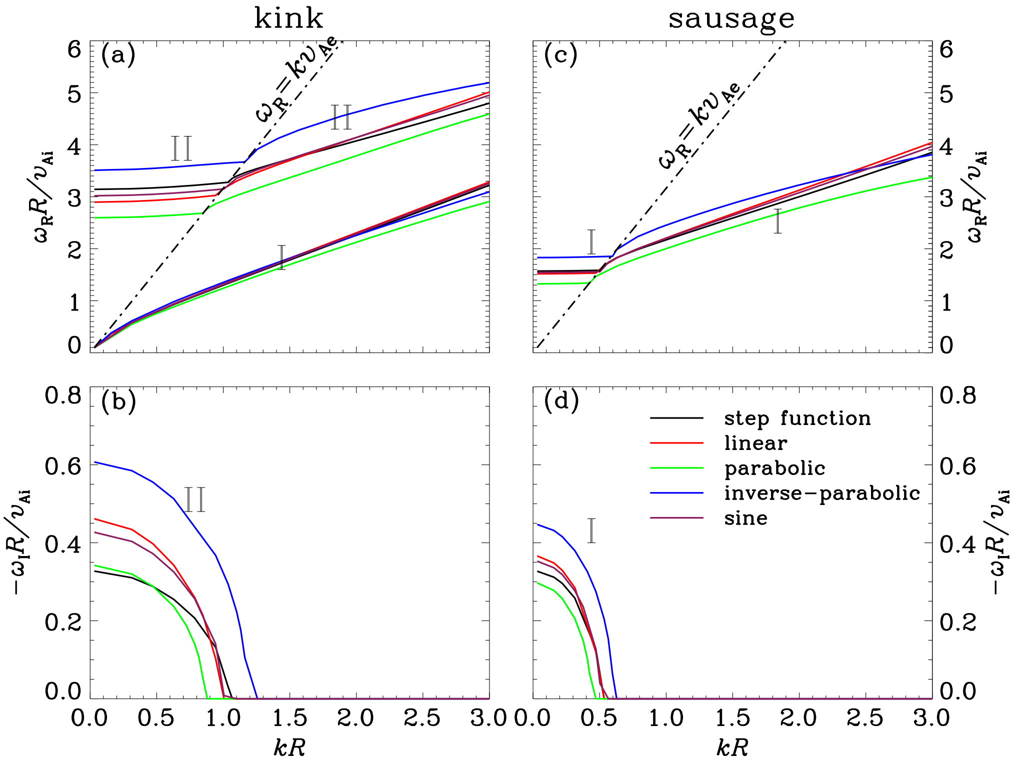

Figure 2. Dispersion diagrams for standing kink (left) and sausage (right) modes in nonuniform slabs. The real (ω_R, the upper row) and imaginary (ω_I, lower row) parts of angular frequency are shown as functions of the real longitudinal wavenumber k. These solutions are found by solving the dispersion relation (Equation (17)) for four different density profiles as represented by the curves in different colors. The corresponding result for a step function profile is given by the black solid curves for comparison. In (a) and (c), the black dashed–dotted lines represent $\omega_R = k v_{Ae}$ and separate the trapped (to its right) from leaky (left) regimes. Here the width of the transition layer $l = R$ and the density contrast $\rho_i/\rho_e = 10$.

3. NUMERICAL RESULTS

3.1. Overview of Dispersion Diagrams

Let us start with an overview of the dispersion diagrams representing the solutions to the DR. Figure 2 presents the dependence on longitudinal wavenumber k of the real (ω_R, the upper row) and imaginary (ω_I, lower) parts of angular frequency for kink (the left column) and sausage (right) modes. Note that $-\omega_I$ is plotted instead of ω_I since $\omega_I \leqslant 0$. For illustration purposes, a combination of $[\rho_i/\rho_e, l/R] = [10, 1]$ is chosen. Four different choices of density profiles are presented in different colors as labeled, and the results pertinent to the step function case are presented by the black solid curves for comparison. The dashed–dotted lines in Figures 2(a) and (c) represent $\omega_R = k v_{Ae}$ and separate the trapped (to their right) from leaky modes (left). There are an infinite number of solutions given the transcendental nature of Equation (17). Therefore, for kink modes we choose to examine only the first two branches (labeled I and II), whereas for sausage modes we examine only the first one (labeled I).

Consider kink modes first. The branches labeled I in Figure 2(a) always lie below the dashed–dotted line, and the associated ω_I is zero (not shown). Hence, these solutions pertain to trapped modes regardless of longitudinal wavenumber. Comparing the black solid line with those in various colors, one finds that for the parameters examined here, the difference introduced by replacing the step function profile with the examined continuous profiles seems marginal. As for the branches labeled II, one sees from Figure 2(a) that common to all profiles, ω_R monotonically decreases with decreasing k, and its k dependence in the leaky regime is substantially weaker than in the trapped one. Likewise, Figure 2(b) indicates that regardless of specific profiles, $|\omega_I|$ monotonically increases with decreasing k once entering the leaky regime. However, the specific values of ω_R and ω_I for branches II show some considerable profile dependence. In the leaky regime, Figure 2(a) indicates that ω_R may be larger or less than in the step function case, which occurs in conjugation with the changes in the critical longitudinal wavenumbers (k_c) corresponding to the intersections between the solid curves and the dashed–dotted one. For instance, one finds that for the parabolic (inverse-parabolic) profile, $\omega_R R/v_{Ai}$ reads 2.6 (3.51) when $kR \rightarrow 0$, while $k_c R$ attains 0.86 (1.19). These values are substantially different from those in the step function case, where $\omega_R R/v_{Ai}$ attains π at $kR \rightarrow 0$, and $k_c R$ is found to be 1.05 (see Equation (20)). Examining Figure 2(b), one sees that the profile dependence of ω_I is even more prominent. Furthermore, take the values at $kR \rightarrow 0$ for example. One finds that $\omega_I R/v_{Ai}$ attains -0.33 in the step function case, but reads -0.61 when the inverse-parabolic profile is chosen.

Now consider the sausage modes given in the right column. Interestingly, the overall dependence of ω on k is similar to the one for kink modes. In particular, the k dependence for continuous profiles is reminiscent of the step function case. However, choosing different density profiles has a considerable impact on the specific values of both ω_R and ω_I. Examine $k \rightarrow 0$ for instance. While in the step function case $[\omega_R, -\omega_I] R/v_{Ai}$ is $[\pi/2, 0.33]$ (see Equation (19)), it attains [1.33, 0.3] and [1.83, 0.45] for the parabolic and inverse-parabolic profiles, respectively.

As discussed in Terradas et al. (2007) pertinent to the cylindrical case with a step function density profile, not all

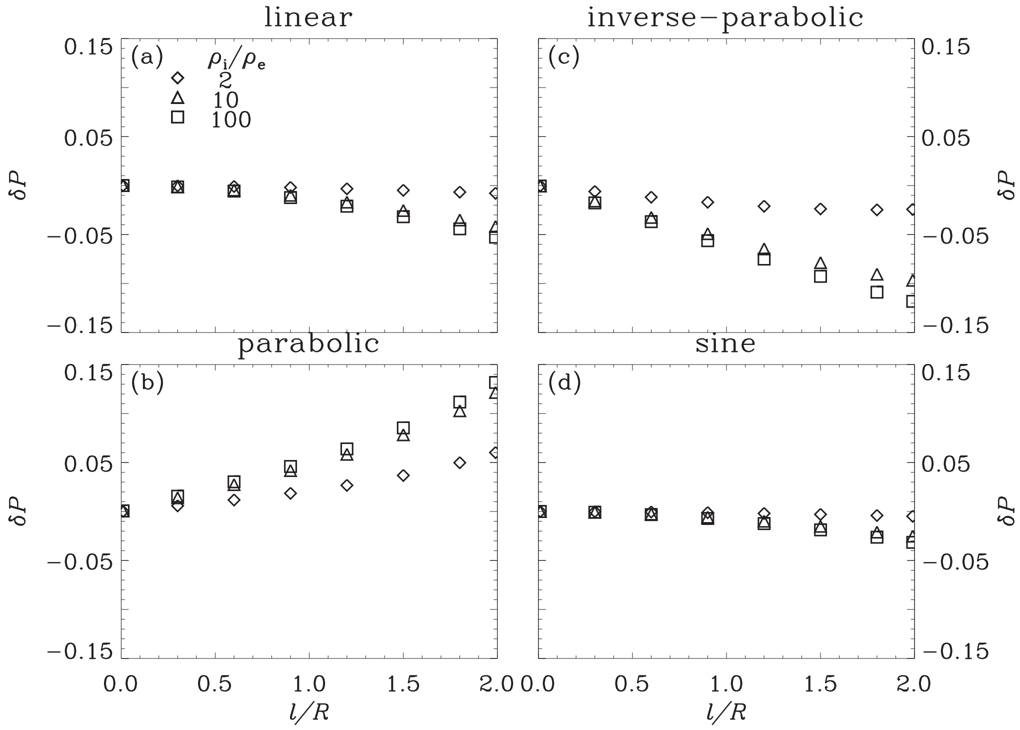

Figure 3. Influence of density profiles on the periods P of standing kink modes labeled I in Figure 2. These modes are trapped at arbitrary longitudinal wavenumber k. Here δP measures the most significant deviation of P from the step function case when kR varies between 0 and 0.2π. A number of density contrasts are examined and represented by different symbols as labeled.

solutions in an eigenmode analysis have physical relevance. Similar to that study (also see Terradas et al. 2005), we approach this issue by solving the relevant time-dependent equations and then asking whether the solutions given in Figure 2 are present in the temporal evolution of the perturbations. In order not to digress from the eigenmode analysis too far, we present the details in Appendix A and simply remark here that the solutions to the DRs as presented in Figure 2 are all physically relevant.

3.2. Standing Kink Modes

This section focuses on how different choices of the $\rho_{\rm tr}$ profile impact the dispersive properties of standing kink modes. Let us start with an examination of this influence on the modes labeled I in Figure 2, which is trapped for arbitrary longitudinal wavenumber k. To proceed, we note that for typical active region (AR) loops, the ratio of half-width to length (R/L) tends to be $\lesssim 0.1$ (e.g., Figure 1 in Schrijver 2007). Even for relatively thick flare loops, R/L does not tend to exceed 0.2 (Nakariakov et al. 2003; Aschwanden et al. 2004). We therefore ask how much the periods P for various density profiles can deviate from the step function counterpart ($P^{\rm step}$) by surveying $kR = \pi R/L$ in the range between 0 and 0.2π. Let δP denote the most significant value attained by $P/P^{\rm step} - 1$ in this range of kR. Figure 3 presents δP as a function of l/R for a number of density contrasts ρ_i/ρ_e as labeled. The results for different density profiles are presented in different panels. One sees that the sign of δP critically depends on the prescription of the density profile. While P is larger than in the step function case for the parabolic profile, it is smaller for the rest of the density profiles. In addition, $|\delta P|$ tends to increase with increasing ρ_i/ρ_e when l/R is fixed. This tendency somehow levels off when ρ_i/ρ_e is large, as evidenced by the fact that the results for $\rho_i/\rho_e = 10$ are close to those for $\rho_i/\rho_e = 100$. Nonetheless, $|\delta P|$ is consistently smaller than 13.2%. As a matter of fact, when linear and sine profiles are adopted, $|\delta P|$ is no larger than 5.3%. From this we conclude that at least for the prescriptions we adopt for the equilibrium density profile, one can use the simpler dispersion relation for the step function case to describe the periods of the first branch of kink modes.

What will be the influence of density profiles on the kink modes labeled II in Figure 2? Figure 4 quantifies this influence by presenting the distribution in the [l/R, ρ_i/ρ_e] plane of the period P (the left column) and damping-time-to-period ratio $\tau/P = \omega_R/|2\pi\omega_I|$ (right), both evaluated at $k = 0$. Here ρ_i/ρ_e is taken to be in the range [2, 200], encompassing the values for both AR loops and flare loops, and τ/P is examined in place of τ since it is a better measure of signal quality. Each row represents one of the four examined density profiles, and the red contours in the right column represents where $\tau/P = 3$, the nominal value required for a temporally damping signal to be measurable. Consider the left column first. When $l/R \to 0$, P attains 2 in all cases, as expected for the step function case where $\omega_R = \pi$ regardless of density contrasts (see Equation (20)). However, some considerable difference appears when continuous profiles are adopted. The period P may be as large as 3.2 for the parabolic profile (the lower right corner in Figure 4(b)). It may also be as small as 1.76, attained for the inverse-parabolic profile (the upper middle part in Figure 4(c)). The l/R-dependence of P is also sensitive to the choice of profiles. With the exception of the inverse-parabolic profile, P monotonically increases with increasing l/R at a fixed density contrast. However, when the inverse-parabolic profile is chosen, P shows a nonmonotonical dependence on l/R, decreasing with l/R first before increasing again. Now examine the right column. One sees that regardless of profiles, τ/P

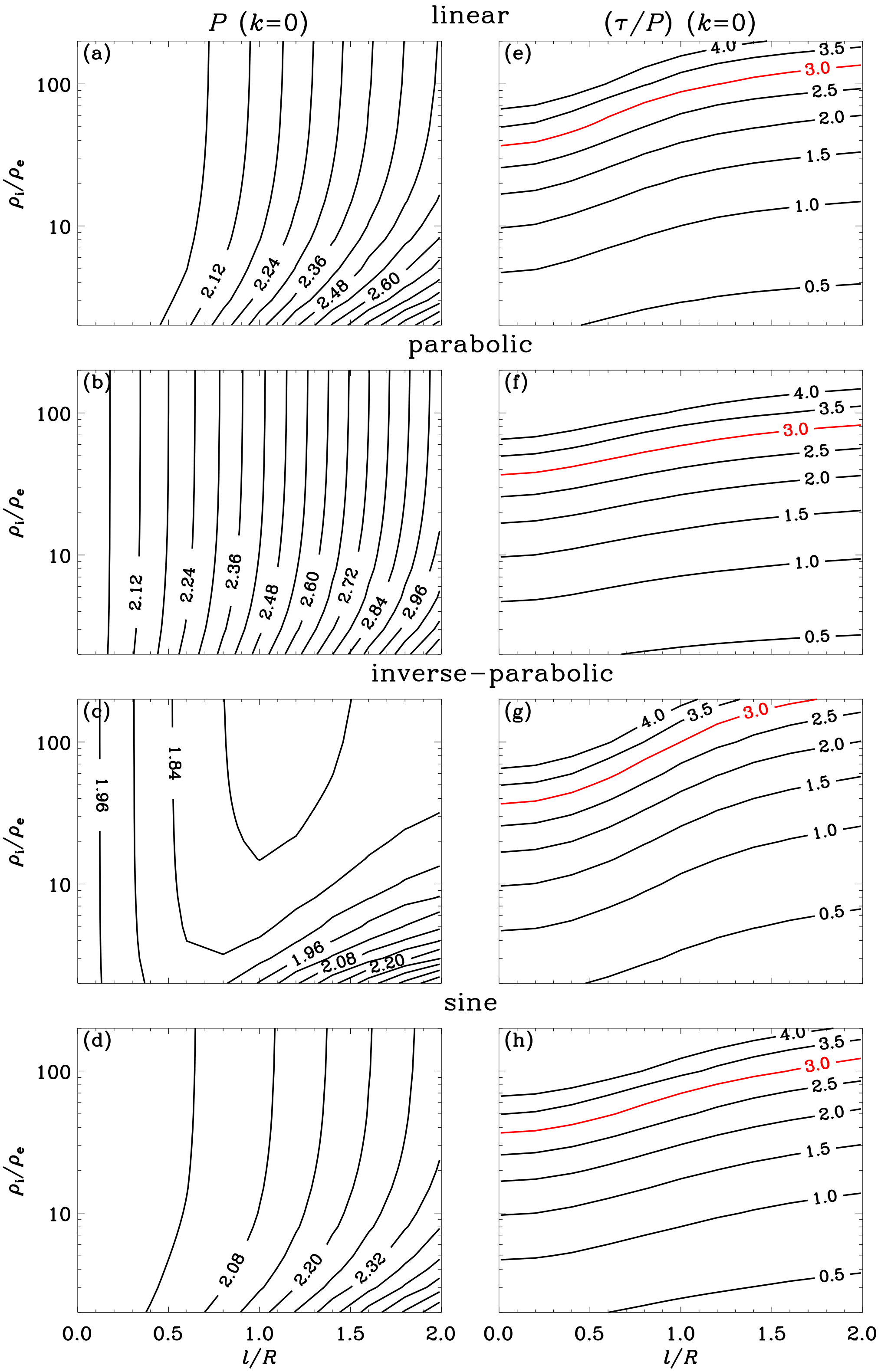

Figure 4. Influence of density profiles on the periods P (left column) and damping-time-to-period ratios τ/P (right) of standing kink modes labeled II in Figure 2. These modes are leaky for small longitudinal wavenumbers k. Contour plots in the $[l/R, \rho_i/\rho_e]$ space are shown for P and τ/P evaluated at $k = 0$. Each row represents one of the four different density profiles as labeled. The red curves in the right column represent where $\tau/P = 3$, the nominal value required for a signal to be observationally discernible.

decreases monotonically with l/R when ρ_i/ρ_e is fixed. This is intuitively expected since more diffuse slabs should be less efficient in trapping wave energy. Nevertheless, the values of τ/P are considerably different for different choices of profiles. Compare the parabolic and inverse-parabolic profiles and examine the intersections between the red curve and the

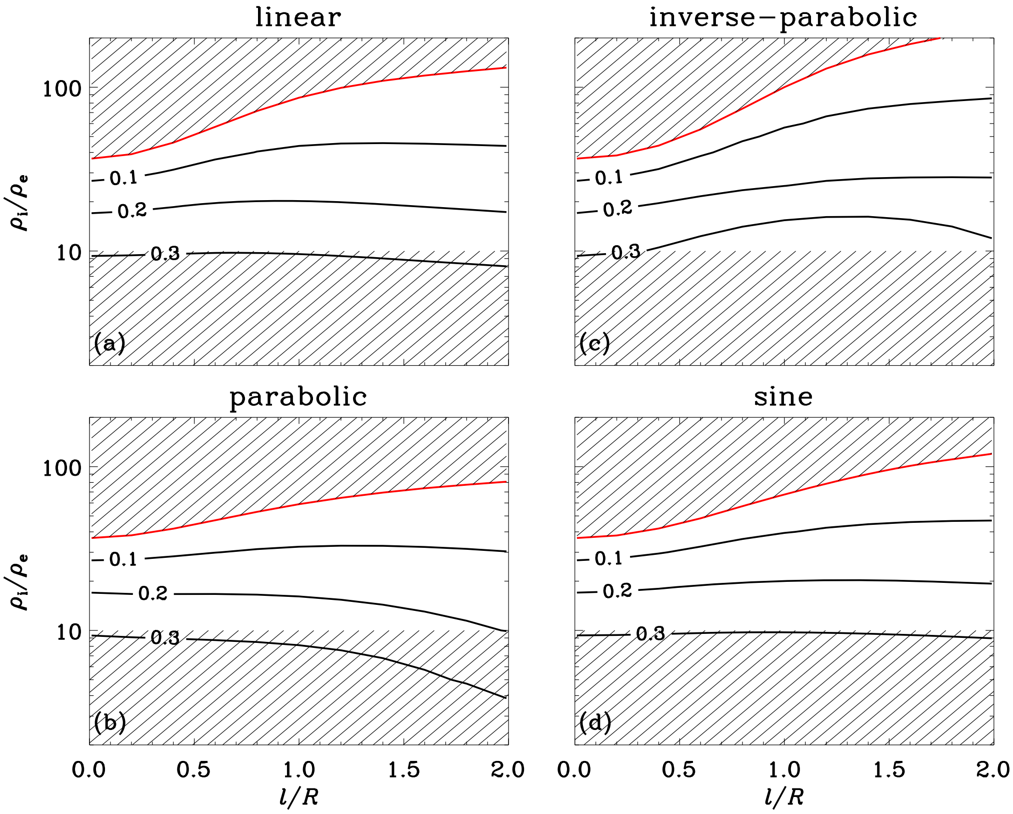

Figure 5. Observability of standing kink modes labeled II in Figure 2. Contour plots in the $[l/R, \rho_i/\rho_e]$ space are shown for $(R/L)_{obs}$ at which the damping-time-to-period ratio τ/P attains three for a given pair of $[l/R, \rho_i/\rho_e]$. The red curve in each panel represents where τ/P at $k = 0$ attains three. In the hatched area bounded from below by this curve, standing kink modes labeled II have sufficiently high quality to be observable, regardless of the geometrical size of slabs. The lower hatched area represents where $\rho_i/\rho_e \leqslant 10$, representative of density contrasts of active region loops. See the text for details.

vertical line representing $l/R = 2$ for instance. While for the parabolic profile this intersection corresponds to $\rho_i/\rho_e = 81$, a value of $\rho_i/\rho_e = 227$ is found for the inverse-parabolic distribution. Actually, this value is beyond the range we adopt for plotting Figure 4.

A question now arises: under what conditions can branch II have sufficiently high quality to be observable? As shown in Figure 2, with decreasing kR, ω_R ($|\omega_I|$) decreases (increases) monotonically, meaning that $\omega_R/|\omega_I|$ and consequently τ/P decrease monotonically. This suggests that for τ/P to exceed a given value $(\tau/P)_{obs}$, taken here to be 3 as required by observations to discern a temporally decaying signal, $R/L = kR/\pi$ has to exceed some critical value $(R/L)_{obs}$. Figure 5 shows the contours of $(R/L)_{obs}$ in the $[l/R, \rho_i/\rho_e]$ plane for different density profiles as given in different panels. In each panel, a contour represents the lower limit of ρ_i/ρ_e for a given l/R for the signals associated with branch II to be observable when the half-width-to-length ratio R/L is smaller than the value given by this contour. Put another way, branch II is observable in the area below a contour only when R/L exceeds at least the value represented by this contour. The red line represents where $(\tau/P)(k = 0) = 3$, meaning that branch II is always observable in the hatched area bounded from below by this red curve. Evidently, this hatched area corresponds to high-density contrasts exceeding at least 36.7, which is attained when $l/R \to 0$ (see Equation (20)). These high-density contrasts are not unrealistic but lie in the observed range of flare or post-flare loops, for which ρ_i/ρ_e may reach up to 10^3 (e.g., Aschwanden et al. 2004). The lower hatched area corresponds to density contrasts characteristic of AR loops, for which $2 \leqslant \rho_i/\rho_e \leqslant 10$ (e.g., Aschwanden et al. 2004). One sees that in this area, for branch II to be observable, the magnetic structures are required to have an R/L exceeding at least 0.2 (see the parabolic profile). In reality, however, R/L for AR loops is $\lesssim 0.1$ (e.g., Schrijver 2007). Therefore, we conclude that branch II is observationally discernible only for flare or post-flare loops.

3.3. Standing Sausage Modes

Now move on to the sausage modes. Figure 6 presents, in the same format as Figure 4, the periods (P, left column) and damping-time-to-period ratios (τ/P, right) at $k = 0$ for various density profiles as given in different rows. The red curves in the right column correspond to $\tau/P = 3$. Consider the left column first. One sees that with the exception of the inverse-parabolic profile, P is consistently larger than in the step function case where $P = 4\ R/v_{Ai}$ (see Equation (19)). It may reach up to $6.09\ R/v_{Ai}$ for the parabolic profile (the lower right corner in Figure 6(b)). Furthermore, for these profiles P monotonically increases with l/R. In other words, the period of sausage modes increases when a slab becomes more diffuse, which agrees with Hornsey et al. (2014) where a specific continuous density profile is chosen. However, this tendency is not universally valid. For instance, for the inverse-parabolic profile, P decreases with l/R in a substantial fraction of the parameter space. In this case, P is consistently smaller than in the step function case and reaches $3.14\ R/v_{Ai}$ at the upper right corner in Figure 6(c). Examining the right column, one finds that while τ/P monotonically decreases with l/R at any given

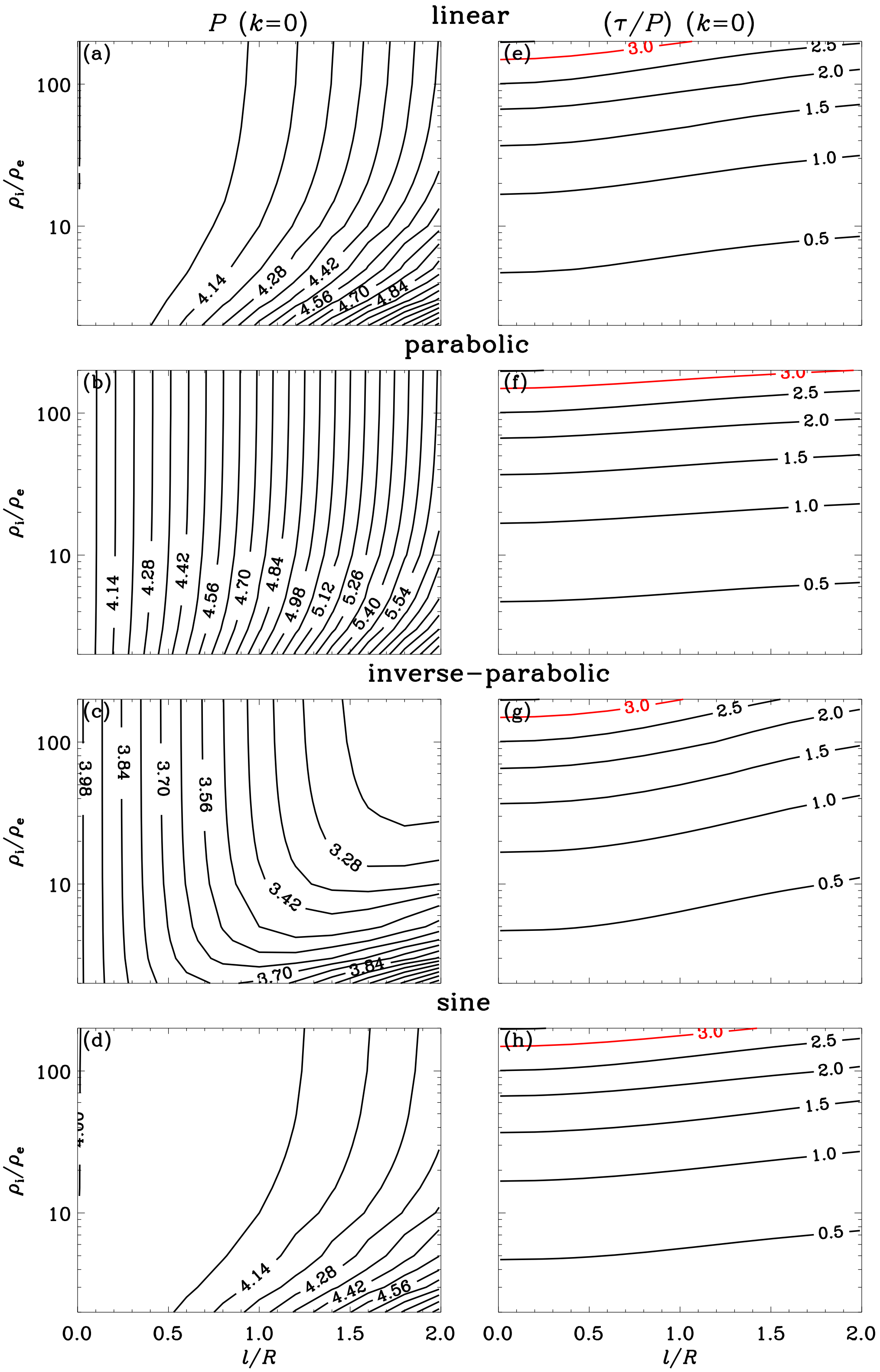

Figure 6. Similar to Figure 4 but for standing sausage modes.

density contrast for all profiles, the specific values of τ/P show some considerable profile dependence. Compare the parabolic and inverse-parabolic profiles and examine the intersections between the red curves and the horizontal lines representing $\rho_i/\rho_e = 200$. One finds that this intersection takes place at an l/R of 1.96 for the parabolic profile, whereas it is located at $l/R = 1.02$ for the inverse-parabolic one.

One may also question whether the sausage modes can be observed. Similar to Figure 5, Figure 7 presents the distribution of $(R/L)_{\rm obs}$ in the $[l/R, \rho_i/\rho_e]$ space, where $(R/L)_{\rm obs}$ represents

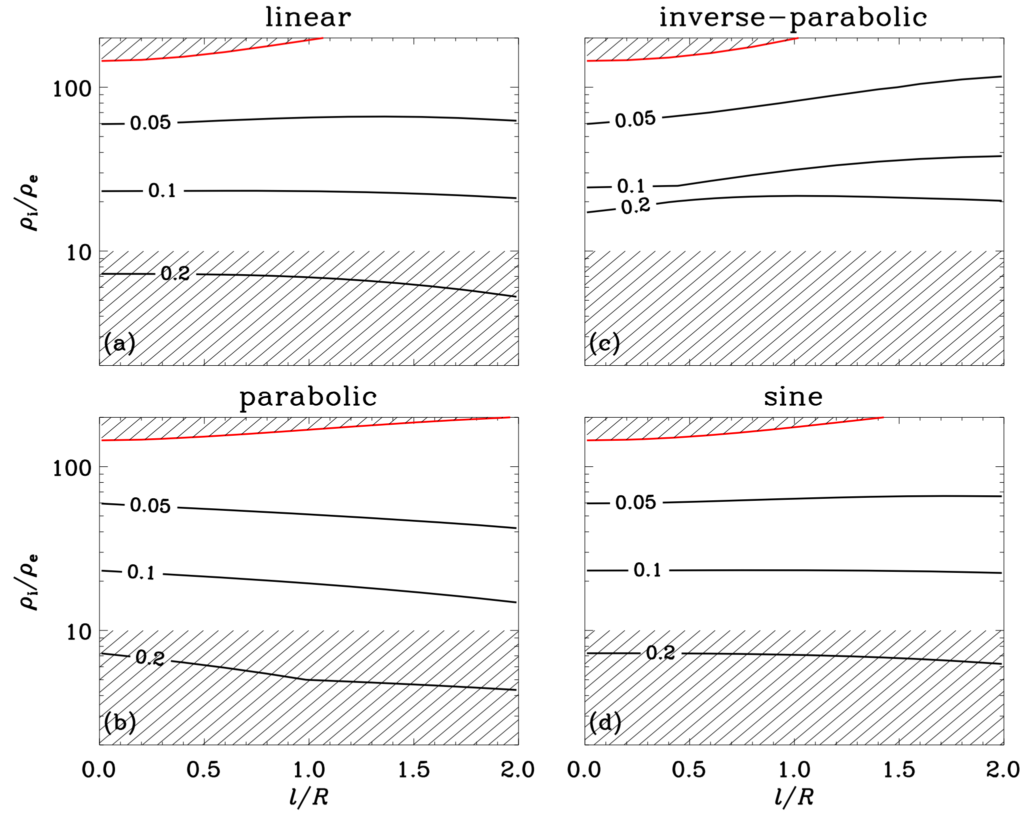

Figure 7. Similar to Figure 5 but for standing sausage modes.

the half-width-to-length ratio at which $\tau/P = 3$. Note that the red curves represent where $(\tau/P)(k=0) = 3$, meaning that slabs with parameters in the hatched part bounded from below by a red curve always support sausage modes with sufficiently high quality, irrespective of their widths or lengths. One sees that this area corresponds to density contrasts that are even higher than for the kink modes. Even when $l/R \to 0$, $\rho_\mathrm{i}/\rho_\mathrm{e}$ needs to be larger than 144 (see Equation (19), and note that $\tau/P \approx \sqrt{\rho_\mathrm{i}/\rho_\mathrm{e}}/4$ for large $\rho_\mathrm{i}/\rho_\mathrm{e}$). However, the severe restriction on $\rho_\mathrm{i}/\rho_\mathrm{e}$ is alleviated given the finite R/L for flare and post-flare loops. Consider the worst case scenario, which takes place for the inverse-parabolic profile. If a slab corresponds to $R/L = 0.2$, then $\rho_\mathrm{i}/\rho_\mathrm{e}$ is required to be larger than only ∼21, which actually lies close to the lower limit of density ratios measured for flare loops (e.g., Aschwanden et al. 2004). When it comes to density contrasts characteristic of AR loops, represented by the lower hatched area, one finds that R/L has to be consistently larger than 0.1 for the sausage modes to be observable. This value, however, is beyond the upper limit of the ratios of half-width to length for AR loops. We therefore conclude that the sausage modes are observable only for flare or post-flare loops.

4. CONCLUSIONS

How plasma density is structured across various magnetic structures in the solar corona remains largely unknown. The present study was intended to examine the influence of continuous transverse density structuring on fast kink and sausage modes collectively supported by coronal slabs. To this end, we worked in the framework of linearized, ideal, cold (zero-β) MHD and modeled coronal loops as straight slabs with a rather general transverse density profile, with the only requirement that the density is uniform beyond some distance from the slab. Analytical DRs governing both fast kink and sausage waves were derived by solving the perturbation equations in terms of regular series expansions in the nonuniform part of the density distribution. The solutions to the DRs were numerically found, and they were shown to be physically relevant in that they are present in the associated time-dependent computations. While one class of density profiles was examined in detail where a transition layer connects a uniform core and an external uniform medium, we showed that a similar analysis is straightforward for density profiles without a uniform core.

Focusing on fundamental standing modes, we found that their periods P (and damping times τ if the modes are leaky) in units of R/v_Ai depend on a combination of dimensionless parameters $[kR, l/R, \rho_\mathrm{i}/\rho_\mathrm{e}]$ once a description for the transverse density profile is prescribed. Here R denotes the slab half-width, v_Ai is the Alfvén speed at the slab axis, k is the longitudinal wavenumber, l is the transverse density length scale, and $\rho_\mathrm{i}/\rho_\mathrm{e}$ is the density contrast between the slab and its surrounding fluid. The lowest order kink modes are trapped for arbitrary k. For the profiles examined, their periods differ by $\lesssim 13\%$ from the case where the transverse density distribution is a step function one when k is in the observed range. However, sausage modes and other branches of kink modes are leaky at small k, and their periods and damping times are sensitive to the choice of the transverse density profile, in particular the density length scale. We also found that these fast modes have sufficiently high quality to be observable only for parameters representative of flare loops.

While the transverse density distribution is allowed to be arbitrary, our analysis nonetheless has a number of limitations.

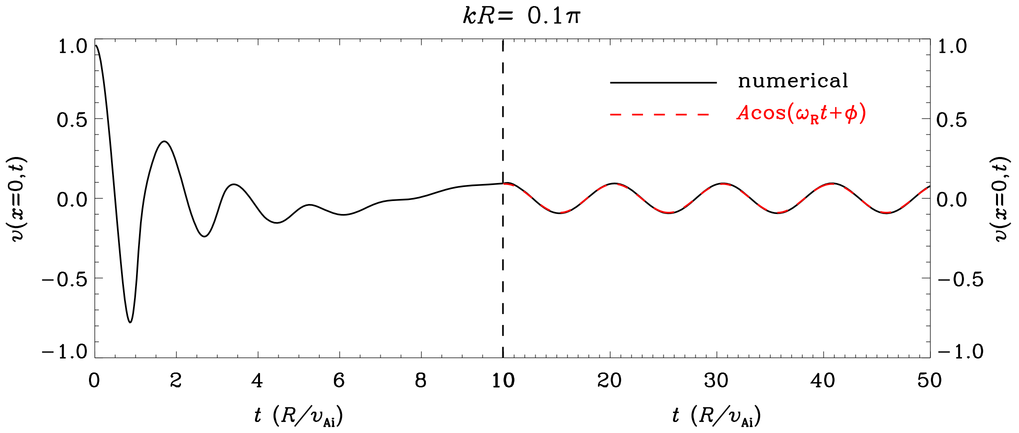

Figure 8. Temporal evolution of transverse velocity perturbation $v\ (x = 0,\ t)$ (the black curve) associated with kink modes supported by a slab with an inverse-parabolic density profile characterized by $\rho_i/\rho_e = 10$ and $l/R = 1$. Here the longitudinal wavenumber $k = 0.1\pi/R$. The red dashed curve represents a fit to the time-dependent solution of the form $A\cos(\omega_R t + \phi)$, where ω_R is found from the eigenmode solution labeled I in Figure 2(a). A different scale is used for the horizontal axis for $t < 10R/v_{Ai}$.

First, we neglected wave propagation out of the plane formed by the slab axis and the direction of density inhomogeneity and therefore cannot address the possible coupling to shear Alfvén waves (e.g., Tirry et al. 1997). Second, the adopted ideal MHD approach excluded the possible role of dissipative mechanisms like magnetic resistivity and ion viscosity in damping the fast modes. In the cylindrical case, resistivity is known to be important for kink modes only in the layer where resonant coupling takes place, and it influences only the detailed structure of the eigenfunctions instead of the damping time or period (e.g., Soler et al. 2013). On the other hand, ion viscosity or electron heat conduction is unlikely to be important for at least some observed sausage modes (e.g., Kopylova et al. 2007). For wave modes in coronal slabs, ion viscosity was shown to be effective only for waves with frequencies exceeding several Hz (Porter et al. 1994). Third, this study neglected the longitudinal variations in plasma density or magnetic field strength. While these effects are unlikely to be important for sausage modes (Pascoe et al. 2009), they may need to be addressed for kink ones, especially when the period ratios between the fundamental mode and its harmonics are used for seismological purposes (e.g., Donnelly et al. 2007).

We thank the referee for the constructive comments. This work is supported by the 973 program 2012CB825601, the National Natural Science Foundation of China (41174154, 41274176, and 41474149), and by the Provincial Natural Science Foundation of Shandong via Grant JQ201212.

APPENDIX A
FAST WAVES IN NONUNIFORM SLABS: AN INITIAL-VALUE-PROBLEM APPROACH

This section demonstrates the physical relevance of the solutions found from the eigenmode analysis. This is done by asking whether the values given by the solid lines in Figure 2 are present in time-dependent solutions. We note that a similar study was conducted for step function density profiles by Terradas et al. (2005, hereafter TOB05). To start, we note that an equation governing the transverse velocity perturbation $\delta v_x(x,\ z,\ t)$ can be readily derived from the linearized, time-dependent, cold MHD equations. Formally expressing $\delta v_x\ (x,\ z,\ t)$ as $v(x,\ t)\sin(kz)$, one finds that $v\ (x,\ t)$ is governed by (e.g., TOB05)

$$\frac{\partial^2 v(x,\ t)}{\partial t^2} = v_A^2(x)\left(\frac{\partial^2}{\partial x^2} - k^2\right)v(x,\ t). \tag{21}$$

When supplemented with appropriate boundary and initial conditions (ICs), Equation (21) can be readily solved such that $v\ (x,\ t)$ at some arbitrarily chosen x can be followed. In practice, it is solved with a simple finite difference code, second order accurate in both space and time, on a uniform grid spanning $[-x_{\rm outer},\ x_{\rm outer}]$ with a spacing $\Delta x = 0.01R$ and $x_{\rm outer} = 500R$. For simplicity, we require that $v\ (x = \pm x_{\rm outer},\ t) = 0$. A uniform timestep Δt is chosen to be $0.8\Delta x/v_{Ae}$ in view of the Courant condition. We have made sure that further refining the grid does not introduce any appreciable change. In addition, the outer boundaries $x = \pm x_{\rm outer}$ are placed sufficiently far from the slab to ensure that the $v\ (x,\ t)$ signals are not contaminated by the perturbations reflected off these boundaries.

Consider kink modes first. To this end, we adopt the following IC

$$v(x,\ t)|_{t=0} = \exp\left[-\left(\frac{x}{R/2}\right)^2\right] - \exp\left[-\left(\frac{x-R}{R/2}\right)^2\right] - \exp\left[-\left(\frac{x+R}{R/2}\right)^2\right],$$

$$\left.\frac{\partial v(x,\ t)}{\partial t}\right|_{t=0} = 0,$$

which represents an initial perturbation of even parity. The solid line in Figure 8 represents the temporal evolution of $v\ (0,\ t)$ for a slab with an inverse-parabolic density profile. Here we choose ρ_i/ρ_e to be 10 and l/R to be 1. In addition, a value of 0.1π is adopted for kR, for which Figures 2(a) and (b) indicate that $\omega_R = 0.616\ v_{Ai}/R$ for branch I, while $[\omega_R,\ \omega_I] = [3.52,\ -0.585]\ v_{Ai}/R$ for branch II. The dashed red line provides a numerical fit to the time-dependent solution with a function of the form $A\cos(\omega_R + \phi)$, where the value for branch I is used for ω_R. Evidently, the solid line for $t \gtrsim 10\ R/v_{Ai}$ agrees remarkably well with the dashed line, meaning that the

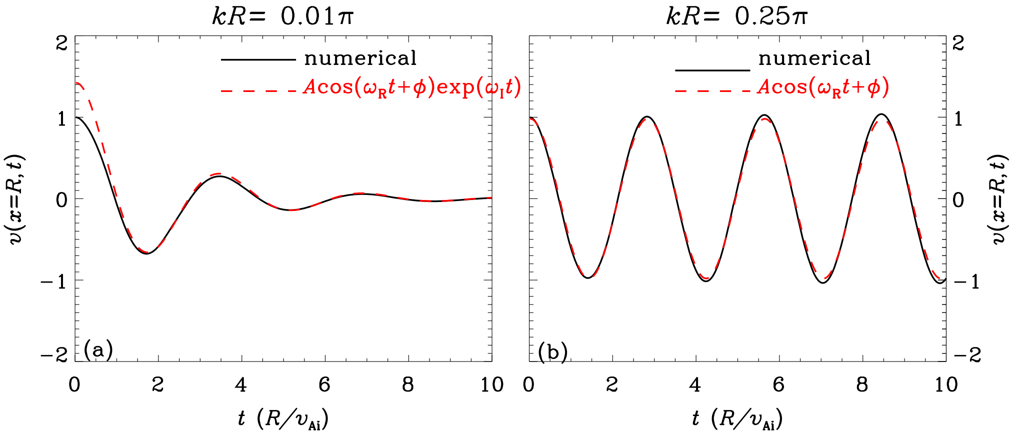

Figure 9. Temporal evolution of transverse velocity perturbations v ($x = R$, t; the black curves) associated with sausage modes supported by a slab with an inverse-parabolic density profile characterized by $\rho_i/\rho_e = 10$ and $l/R = 1$. The results for two different values of the longitudinal wavenumber k, one $0.01\pi/R$ and the other $0.25\ \pi/R$, are given in panels (a) and (b), respectively. The red dashed curves represent a fit in the form $A\cos(\omega_R t + \phi)\exp(\omega_I t)$ where the values for $[\omega_R, \omega_I]$ are obtained from the eigenmode analysis presented in Figures 2(c) and (d). Note that $\omega_I = 0$ when $kR = 0.25\pi$.

signal evolves into the trapped mode found in the eigenmode analysis. Furthermore, a Fourier analysis of the signal for $t \lesssim 10\ R/v_{Ai}$ reveals a periodicity of $1.7 \sim 1.8\ R/v_{Ai}$, or equivalently, an angular frequency of $3.5 \sim 3.7\ v_{Ai}/R$. This is in close accordance with the expectation from the first leaky mode labeled II, even though the signal decays too rapidly for one to determine accurately the period and damping rate. We note that this is why TOB05 called this stage "the impulsive leaky phase," since wave leakage plays an essential role in this evolutionary stage. When compared with Figure 10 in TOB05, our Figure 8 indicates that despite the quantitative differences, the temporal evolution of kink perturbations for diffuse slabs is qualitatively similar to what happens for slabs with a step function form.

We now examine sausage modes by adopting the IC

$$v(x, t)|_{t=0} = \frac{2x/R}{1 + (x/R)^2},$$
$$\left.\frac{\partial v(x, t)}{\partial t}\right|_{t=0} = 0,$$

which represents an initial perturbation of odd parity and localized around $x = \pm R$. The temporal evolution of v (R, t) is presented by the solid lines in Figure 9, where two different values of kR are examined for a slab also characterized by an inverse-parabolic profile with $\rho_i/\rho_e = 10$ and $l/R = 1$. The result for $kR = 0.01\pi$ is shown in Figure 9(a), pertinent to the leaky mode with $[\omega_R, \omega_I] = [1.83, -0.447]\ v_{Ai}/R$ as expected from Figures 2(c) and (d). The red dashed line represents a fit to the time-dependent signal with $A\cos(\omega_R t + \phi)\exp(\omega_I t)$, and is found to agree well with the solid line. On the other hand, Figure 9(b) examines the case where $kR = 0.25\pi$, pertinent to the trapped mode with $\omega_R = 2.23\ v_{Ai}/R$ as expected from Figure 2(c). The red dashed line represents a fit to the time-dependent result with $A\cos(\omega_R + \phi)$. Evidently, the red dashed line is hard to tell apart from the time-dependent result.

To summarize this section, we remark that the perturbations bearing signatures expected from the eigenmode analysis can be readily generated. While the results are shown only at some specific kR for an inverse-parabolic profile with some specific combination of $[l/R,\ \rho_i/\rho_e]$, the same conclusion has been reached when we experiment with all the considered profiles for a substantial range of l/R, ρ_i/ρ_e, and kR.

APPENDIX B
FAST WAVES IN NONUNIFORM SLABS WITHOUT A UNIFORM CORE

In this section we will examine slabs with equilibrium density profiles of the form

$$\rho(x) = \begin{cases} \rho_i + (\rho_e - \rho_i) f(\bar{x}), & 0 \leqslant x < R, \\ \rho_e, & x \geqslant R, \end{cases} \tag{22}$$

where $\bar{x} = x/R$ and $f(\bar{x})$ is an arbitrary function that smoothly connects 0 at $\bar{x} = 0$ to 1 at $\bar{x} = 1$. Redefining ζ as $x - R/2$, the Fourier amplitude of the transverse Lagrangian displacement $\tilde{\xi}_x$ can be expressed as

$$\tilde{\xi}_x(x) = \begin{cases} A_1\tilde{\xi}_1(\zeta) + A_2\tilde{\xi}_2(\zeta), & 0 \leqslant x < R, \\ A_e \exp\left(i\mu_e x\right), & x > R, \end{cases} \tag{23}$$

where A_1, A_2, and A_e are arbitrary constants, while $\tilde{\xi}_1$ and $\tilde{\xi}_2$ represent two linearly independent solutions to Equation (4) for $x < R$. Unsurprisingly, $\tilde{\xi}_1$ and $\tilde{\xi}_2$ are still describable by Equations (6)–(10). The Fourier amplitude of the Eulerian perturbation of the total pressure reads

$$\tilde{p}_{\rm tot}(x) = -\frac{B^2}{4\pi} \times \begin{cases} A_1\tilde{\xi}_1'(\zeta) + A_2\tilde{\xi}_2'(\zeta), & 0 \leqslant x < R, \\ iA_e\mu_e \exp\left(i\mu_e x\right), & x > R. \end{cases} \tag{24}$$

The derivation of the dispersion relation (DR) follows closely the one given in Section 2.3, the only difference being that in place of the interface between a uniform core and the transition layer, the slab axis $x = 0$ needs to be examined. To be specific, $\tilde{\xi}_x$ is required to be of even (odd) parity for kink (sausage) modes

$$A_1\tilde{\xi}_1\left(\zeta_i\right) + A_2\tilde{\xi}_2\left(\zeta_i\right) = 0, \text{ sausage},$$
$$A_1\tilde{\xi}_1'\left(\zeta_i\right) + A_2\tilde{\xi}_2'\left(\zeta_i\right) = 0, \text{ kink }, \tag{25}$$

where $\zeta_\mathrm{i} = -R/2$. On the other hand, the continuity of both $\tilde{\xi}$ and $\tilde{p}_\mathrm{tot}$ at $x = R$ means that

$$\begin{aligned} A_1 \tilde{\xi}_1(\zeta_\mathrm{e}) + A_2 \tilde{\xi}_2(\zeta_\mathrm{e}) &= A_\mathrm{e} \exp(i\mu_\mathrm{e} R), \\ A_1 \tilde{\xi}_1'(\zeta_\mathrm{e}) + A_2 \tilde{\xi}_2'(\zeta_\mathrm{e}) &= iA_\mathrm{e}\mu_\mathrm{e} \exp(i\mu_\mathrm{e} R), \end{aligned}$$

where $\zeta_\mathrm{e} = R/2$. Eliminating A_e, one finds that

$$\frac{A_1 \tilde{\xi}_1'(\zeta_\mathrm{e}) + A_2 \tilde{\xi}_2'(\zeta_\mathrm{e})}{A_1 \tilde{\xi}_1(\zeta_\mathrm{e}) + A_2 \tilde{\xi}_2(\zeta_\mathrm{e})} = i\mu_\mathrm{e}. \tag{26}$$

The algebraic equations governing A_1 and A_2 then follow from Equations (25) and (26)

$$\begin{aligned} \Lambda_1 A_1 + \Lambda_2 A_2 &= 0 \\ \Lambda_3 A_1 + \Lambda_4 A_2 &= 0, \end{aligned} \tag{27}$$

with

$$\Lambda_1 = \begin{cases} \tilde{\xi}_1(\zeta_\mathrm{i}), & \text{sausage} \\ \tilde{\xi}_1'(\zeta_\mathrm{i}), & \text{kink} \end{cases} \quad \Lambda_2 = \begin{cases} \tilde{\xi}_2(\zeta_\mathrm{i}), & \text{sausage} \\ \tilde{\xi}_2'(\zeta_\mathrm{i}), & \text{kink} \end{cases}$$
$$\Lambda_3 = i\mu_\mathrm{e}\tilde{\xi}_1(\zeta_\mathrm{e}) - \tilde{\xi}_1'(\zeta_\mathrm{e}), \quad \Lambda_4 = i\mu_\mathrm{e}\tilde{\xi}_2(\zeta_\mathrm{e}) - \tilde{\xi}_2'(\zeta_\mathrm{e}). \tag{28}$$

For $[A_1, A_2]$ not to be identically zero, one needs to require that

$$\Lambda_1\Lambda_4 - \Lambda_2\Lambda_3 = 0, \tag{29}$$

which is the DR governing fast waves supported by magnetic slabs with equilibrium density profiles described by Equation (22).

What happens for a step function form of the density profile? This may take place, for instance, when $f(\bar{x}) = \bar{x}^\mu$ with $\mu \to \infty$. In this case one finds that $\rho_0 = \rho_\mathrm{i}$ and $\rho_n = 0$ for $n \geqslant 1$. Equation (10) then leads to that $a_n = 0$ for odd n, whereas for even $n = 2m$ $(m = 1, 2, \ldots)$,

$$a_{2m} = (-1)^m \frac{\mu_\mathrm{i}^{2m}}{(2m)!} a_0,$$

meaning that $\tilde{\xi}_1$ can be expressed as

$$\tilde{\xi}_1 = a_0 \sum_{m=0}^{\infty} (-1)^m \frac{\mu_\mathrm{i}^{2m}}{(2m)!} \zeta^{2m} = a_0 \cos(\mu_\mathrm{i}\zeta). \tag{30}$$

Note that $a_0 \neq 0$ but $a_1 = 0$. Likewise, by noting that $b_0 = 0$ but $b_1 \neq 0$, one finds that $b_n = 0$ for even n, whereas for odd $n = 2m + 1$ $(m = 1, 2, \ldots)$,

$$b_{2m+1} = (-1)^m \frac{\mu_\mathrm{i}^{2m}}{(2m+1)!} b_1.$$

As a result,

$$\tilde{\xi}_2 = b_1 \sum_{m=0}^{\infty} (-1)^m \frac{\mu_\mathrm{i}^{2m}}{(2m+1)!} \zeta^{2m+1} = \frac{b_1}{\mu_\mathrm{i}} \sin(\mu_\mathrm{i}\zeta). \tag{31}$$

Evaluating the coefficients Λ_n $(n = 1, \ldots, 4)$ in Equation (29) with the explicit expressions for $\tilde{\xi}_1$ and $\tilde{\xi}_2$, one finds that for sausage waves

$$\begin{aligned} 0 &= i\mu_\mathrm{e}\left[2\sin(\mu_\mathrm{i}R/2)\cos(\mu_\mathrm{i}R/2)\right] \\ &\quad - \mu_\mathrm{i}\left[\cos^2(\mu_\mathrm{i}R/2) - \sin^2(\mu_\mathrm{i}R/2)\right] \\ &= i\mu_\mathrm{e}\sin(\mu_\mathrm{i}R) - \mu_\mathrm{i}\cos(\mu_\mathrm{i}R), \end{aligned}$$

thereby recovering the step function case (see, for example, Equation (18)). The DR for kink waves can be simplified in a similar fashion. Finally, let us note that although $\tilde{\xi}_1(\zeta)$ $(\tilde{\xi}_2(\zeta))$ is an even (odd) function, it is not so when $x = \zeta + R/2$ is seen as the independent variable. However, some algebra using trigonometric identities shows that the combination of the two $(A_1\tilde{\xi}_1 + A_2\tilde{\xi}_2)$ is proportional to $\sin(\mu_\mathrm{i}x)$ $(\cos(\mu_\mathrm{i}x))$ for sausage (kink) waves, thereby explicitly showing the parity of the eigenfunctions implied by Equation (25).

For simplicity, we have explored only one specific $f(\bar{x})$, namely $\bar{x}^\mu$ with μ positive. Rather than further presenting dispersion diagrams showing the solutions to Equation (29), let us remark that these solutions behave in a manner qualitatively similar to the ones presented in Figure 2 and their physical relevance can also be demonstrated by time-dependent computations.

REFERENCES

Arregui, I., Andries, J., Van Doorsselaere, T., Goossens, M., & Poedts, S. 2007, A&A, 463, 333
Aschwanden, M. J., Nakariakov, V. M., & Melnikov, V. F. 2004, ApJ, 600, 458
Ballester, J. L., Erdélyi, R., Hood, A. W., Leibacher, J. W., & Nakariakov, V. M. 2007, SoPh, 246, 1
Banerjee, D., Erdélyi, R., Oliver, R., & O'Shea, E. 2007, SoPh, 246, 3
Cally, P. S. 1986, SoPh, 103, 277
Chen, S.-X., Li, B., Xia, L.-D., & Yu, H. 2015a, SoPh, 290, 2231
Chen, S.-X., Li, B., Xiong, M., Yu, H., & Guo, M.-Z. 2015b, ApJ, 812, 22
Chen, Y., Feng, S. W., Li, B., et al. 2011, ApJ, 728, 147
Chen, Y., Song, H. Q., Li, B., et al. 2010, ApJ, 714, 644
De Moortel, I., & Nakariakov, V. M. 2012, RSPTA, 370, 3193
Donnelly, G. R., Díaz, A. J., & Roberts, B. 2007, A&A, 471, 999
Edwin, P. M., & Roberts, B. 1982, SoPh, 76, 239
Edwin, P. M., & Roberts, B. 1983, SoPh, 88, 179
Edwin, P. M., & Roberts, B. 1988, A&A, 192, 343
Edwin, P. M., Roberts, B., & Hughes, W. J. 1986, GeoRL, 13, 373
Erdélyi, R., & Goossens, M. 2011, SSRv, 158, 167
Erdélyi, R., & Taroyan, Y. 2008, A&A, 489, L49
Feng, S. W., Chen, Y., Li, B., et al. 2011, SoPh, 272, 119
Goossens, M., Andries, J., & Aschwanden, M. J. 2002, A&A, 394, L39
Goossens, M., Arregui, I., Ballester, J. L., & Wang, T. J. 2008, A&A, 484, 851
Goossens, M., Erdélyi, R., & Ruderman, M. S. 2011, SSRv, 158, 289
Hollweg, J. V., & Yang, G. 1988, JGR, 93, 5423
Hornsey, C., Nakariakov, V. M., & Fludra, A. 2014, A&A, 567, A24
Jelínek, P., & Karlický, M. 2012, A&A, 537, A46
Karlický, M., Mészárosová, H., & Jelínek, P. 2013, A&A, 550, A1
Kopylova, Y. G., Melnikov, A. V., Stepanov, A. V., Tsap, Y. T., & Goldvarg, T. B. 2007, AstL, 33, 706
Li, B., Chen, S.-X., Xia, L.-D., & Yu, H. 2014, A&A, 568, A31
Li, B., Habbal, S. R., & Chen, Y. 2013, ApJ, 767, 169
Lopin, I., & Nagorny, I. 2015, ApJ, 801, 23
Murawski, K., & Roberts, B. 1993, SoPh, 143, 89
Nakariakov, V. M., Arber, T. D., Ault, C. E., et al. 2004, MNRAS, 349, 705
Nakariakov, V. M., & Erdélyi, R. 2009, SSRv, 149, 1
Nakariakov, V. M., Hornsey, C., & Melnikov, V. F. 2012, ApJ, 761, 134
Nakariakov, V. M., & Melnikov, V. F. 2009, SSRv, 149, 119
Nakariakov, V. M., Melnikov, V. F., & Reznikova, V. E. 2003, A&A, 412, L7
Nakariakov, V. M., & Ofman, L. 2001, A&A, 372, L53
Nakariakov, V. M., & Roberts, B. 1995, SoPh, 159, 399
Nakariakov, V. M., & Verwichte, E. 2005, LRSP, 2, 3
Ofman, L., & Wang, T. J. 2008, A&A, 482, L9
Pascoe, D. J., Nakariakov, V. M., & Arber, T. D. 2007, SoPh, 246, 165

Pascoe, D. J., Nakariakov, V. M., Arber, T. D., & Murawski, K. 2009, A&A, 494, 1119
Porter, L. J., Klimchuk, J. A., & Sturrock, P. A. 1994, ApJ, 435, 502
Roberts, B. 1981a, SoPh, 69, 39
Roberts, B. 1981b, SoPh, 69, 27
Roberts, B., Edwin, P. M., & Benz, A. O. 1984, ApJ, 279, 857
Rosenberg, H. 1970, A&A, 9, 159
Ruderman, M. S., & Roberts, B. 2002, ApJ, 577, 475
Schrijver, C. J. 2007, ApJL, 662, L119
Smith, J. M., Roberts, B., & Oliver, R. 1997, A&A, 327, 377
Soler, R., Goossens, M., Terradas, J., & Oliver, R. 2013, ApJ, 777, 158
Soler, R., Goossens, M., Terradas, J., & Oliver, R. 2014, ApJ, 781, 111
Spruit, H. C. 1982, SoPh, 75, 3
Terradas, J., Andries, J., & Goossens, M. 2007, SoPh, 246, 231
Terradas, J., Oliver, R., & Ballester, J. L. 2005, A&A, 441, 371
Tirry, W. J., Cadez, V. M., & Goossens, M. 1997, A&A, 324, 1170
Uchida, Y. 1970, PASJ, 22, 341
Vasheghani Farahani, S., Hornsey, C., Van Doorsselaere, T., & Goossens, M. 2014, ApJ, 781, 92
Verwichte, E., Nakariakov, V. M., & Cooper, F. C. 2005, A&A, 430, L65
White, R. S., & Verwichte, E. 2012, A&A, 537, A49
Zajtsev, V. V., & Stepanov, A. V. 1975, IGAFS, 37, 3